2022 IEEE International Conference on Robotics and Automation (ICRA)
May 23-27, 2022. Philadelphia, PA, USA

Decoupling of Inertia Effect in Angular Momentum of a Humanoid and its Application to Resolved Viscoelasticity Control

Zewen He and Ko Yamamoto

***Abstract*— As a basic part of the centroidal dynamics, angular momentum plays a critical role in humanoid motion control. Therefore, how to explicitly express and control angular momentum through whole-body motion is an important topic for researchers. This study discusses the selection of the generalized velocity corresponding to whole-body angular momentum. Based on the discussion, we present a method that decouples the inertia effect in centroidal angular momentum and applies it in resolved viscoelasticity control, which achieves the angular momentum control by whole-body compliance in an interpretable way without complicated calculation. At last, we validate the feasibility and effectiveness of proposed method in forward dynamics simulation of balancing control in the double and single support states and landing motion after hopping.**

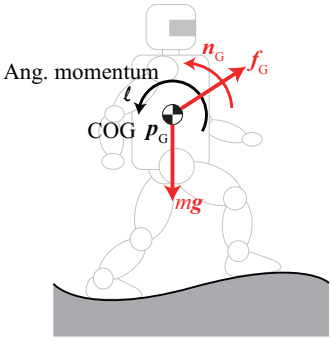


Fig. 1: Centroidal dynamics of a humanoid robot.

I. Introduction

Simplified reduced-dimensional model has been effective in the field of dynamics and control of multiple degree-of-freedom (DOF) rigid-body robotic system such as humanoid robot [1], [2], [3]. Especially on a humanoid robot, the dynamics including contact force can be expressed clearly by considering the motion related to the whole-body center of gravity (COG) and angular momentum (AM) around the COG, which is called centroidal dynamics [4], [5]. Currently many methods to achieve control of centroidal dynamics through whole-body motion have been proposed, such as COG Jacobian control [6], resolved momentum control [7], and the method of using inverse kinematics and inverse dynamcis together [8].

Generally, the AM of a single rigid body is expressed by the product of its inertia and the angular velocity. When considering the AM of the entire multi-rigid-body system, however the effect of inertia term is included in the system AM, which cannot be separated explicitly. Spatial average velocity [5], [9] have been proposed as an angular velocity corresponding to AM, but its physical meaning is rarely considered.

Based on the control of AM or the corresponding spatial average velocity, a humanoid robot can implement the so-called *hip strategy* to keep body balance, which also means using changing rate of AM to make the COG back to its equilibrium. This strategy always combined with other strategies like ankle strategy in humanoid robot control, which is realized in many researches [10], [11], [12], [13], [14]. Because of the nonlinearity of the centroidal dynamics, nonlinear model predictive control (NMPC) becomes an effective controller solved by some quadratic programming (QP) methods in the above researches. In our previous works, resolved viscoelasticity control (RVC) opened the other way based on compliance optimization control to achieve the similar control target [15], [16]. In our previous studies, however, the AM term has not been controlled explicitly nor used in COG feeback control in a decoupled form.

In this paper, we focus on how to select the generalized velocity corresponding to the whole-body AM, and discuss the way to define a generalized velocity that can decouple the effect of inertia term in AM, and the corresponding generalized force. Finally we apply the proposed method into viscoelastic decomposition control [16] related to the COG and AM, and report the verification results on balancing control by using forward dynamics simulation. Compared with other researches on whole-body AM control, the main contribution of this paper includes the following points:

1) Decoupling the inertia effect in whole-body AM analytically to define a generalized velocity and generalized force corresponding to centroidal dynamics, which can avoid double-counting the inertia effect in AM viscoelasticity formulation;
2) Applying the generalized velocity and force in centroidal dynamics control, extending previous RVC into *centroidal viscoelasticity*, which improves the performance of whole-body balance control.

It is worth noting that, in this paper, $\boldsymbol{E}$ is an identity matrix, $\boldsymbol{O}$ a zero matrix, $\mathrm{diag}\{x_i\}$ a diagonal matrix with $x_i (i = 1, \cdots)$ as diagonal element, $\mathrm{diag}\{\boldsymbol{X}_i\}$ a block diagonal matrix with $\boldsymbol{X}_i$ as block element, and $[\boldsymbol{X}\times]$ a skew-symmetric matrix representing cross product. For a physical quantity $*$, $*_{ref}$ represents the target value, and $\Delta * = *_{ref} - *$ represents the error to the target value.

This research is supported by JSPS KAKENHI Grant Number 21H01282.
The authors are with the Department of Mechanical Engineering, Univ. of Tokyo, 7-3-1 Hongo, Bunkyo-ku, Tokyo 113-8656, Japan. he-zewen@ynl.t.u-tokyo.ac.jp

II. Centroidal Dynamics and Jacobian Matrix

A. Centroidal Dynamics

Centroidal dynamics of a humanoid robot shown in Fig. 1 is represented as follows:

$$m\ddot{\boldsymbol{p}}_G = \boldsymbol{f}_G - m\boldsymbol{g} \tag{1}$$

$$\dot{\boldsymbol{\ell}} = \boldsymbol{n}_G \tag{2}$$

where m is the total mass; $\boldsymbol{p}_G \in \mathbb{R}^3$ is the position of the COG; $\boldsymbol{f}_G \in \mathbb{R}^3$ is the force acting on the COG excluding the gravity; $\boldsymbol{\ell} \in \mathbb{R}^3$ is the AM around the COG, represented as follows:

$$\boldsymbol{\ell} = \sum_{i=0}^{n} \{(\boldsymbol{p}_{G,i} - \boldsymbol{p}_G) \times \dot{\boldsymbol{p}}_{G,i} m_i + \boldsymbol{I}_{G,i}\boldsymbol{\omega}_i\}. \tag{3}$$

where $m_i, \boldsymbol{p}_{G,i} \in \mathbb{R}^3, \boldsymbol{I}_{G,i} \in \mathbb{R}^{3\times3}, \boldsymbol{\omega}_i$ are the mass, COG, inertia matrix around the COG, angular velocity of link i, respectively; and $\boldsymbol{n}_G \in \mathbb{R}^3$ is the total moment acting on the COG, represented as follows:

$$\boldsymbol{n}_G = \sum_{i=0}^{n} \{\boldsymbol{n}_i + (\boldsymbol{p}_{G,i} - \boldsymbol{p}_G) \times \boldsymbol{f}_i\} \tag{4}$$

where $\boldsymbol{f}_i, \boldsymbol{n}_i \in \mathbb{R}^3$ are force and moment acting on the COG of link i, respectively.

B. Angular Momentum Jacobian Matrix

Let $\dot{\boldsymbol{q}}$ denote the generalized velocity of the robot. The relationship between the AM $\boldsymbol{\ell}$ and $\dot{\boldsymbol{q}}$ is given as a linear mapping.

$\dot{\boldsymbol{p}}_{G,i}$ and $\boldsymbol{\omega}_i$ are associated with $\dot{\boldsymbol{q}}$ as follows:

$$\dot{\boldsymbol{p}}_{G,i} = \boldsymbol{J}_{G,i}\dot{\boldsymbol{q}}, \tag{5}$$

$$\boldsymbol{\omega}_i = \boldsymbol{J}_{\omega,i}\dot{\boldsymbol{q}} \tag{6}$$

where $\boldsymbol{J}_{G,i}$ is the Jacobian matrix of the COG velocity of link i, and $\boldsymbol{J}_{\omega,i}$ is the basic Jacobian matrix of the angular velocity of link i. Substituting these equations into (3) yields

$$\boldsymbol{\ell} = \underbrace{\sum_i \{m_i(\boldsymbol{p}_{G,i} - \boldsymbol{p}_G) \times \boldsymbol{J}_{G,i} + \boldsymbol{I}_{G,i}\boldsymbol{J}_{\omega,i}\}}_{\boldsymbol{J}_{\mathrm{AM}}} \dot{\boldsymbol{q}} \tag{7}$$

$\boldsymbol{J}_{\mathrm{AM}}$ is called as angular momentum Jacobian matrix [7], [6], [5].

C. Spatial Average Velocity

In a single rigid-body, its AM is represented by the multiplication of the inertial matrix and angular velocity. On the other hand, the AM of a multi-link system cannot be divided into such inertia matrix and velocity. An attempt to define an angular velocity corresponding to $\boldsymbol{\ell}$ is to define *spatial average velocity* [5] as follows:

$$\boldsymbol{\omega}_G := \boldsymbol{I}_G^{-1}\boldsymbol{\ell} \tag{8}$$

where $\boldsymbol{I}_G$ is the total inertia matrix around the COG represented by

$$\boldsymbol{I}_G = \sum_{i=0}^{n} (\boldsymbol{I}_{G,i} + m_i[(\boldsymbol{p}_{G,i} - \boldsymbol{p}_G)\times][(\boldsymbol{p}_{G,i} - \boldsymbol{p}_G)\times]^T) \tag{9}$$

This is the inertia matrix of the composite rigid body [17], which assumes the multi-link system as a single body fixing all joints. Saccon et al. [9] discussed the integrability of $\boldsymbol{\omega}_G$. However, the physical meaning of $\boldsymbol{\omega}_G$ is rarely focused on.

III. Generalized Velocity Corresponding to Angular Momentum

In this section, we discuss about the inertia term in AM, and summarize expression of the generalized velocity corresponding to whole-body AM, which now has two candidates through theoretical derivation.

A. Inertia Effect included in Angular Momentum

The AM $\boldsymbol{\ell}$ is rewritten from (3) as follows:

$$\boldsymbol{\ell} = \mathcal{A}\mathcal{M}\dot{\boldsymbol{\xi}} \tag{10}$$

where $\mathcal{A}, \mathcal{M}$ and $\dot{\boldsymbol{\xi}}$ are defined as follows:

$$\mathcal{A} := \begin{bmatrix}[(\boldsymbol{p}_{G,1} - \boldsymbol{p}_G)\times] & \boldsymbol{E} & \cdots & [(\boldsymbol{p}_{G,n} - \boldsymbol{p}_G)\times] & \boldsymbol{E}\end{bmatrix} \tag{11}$$

$$\mathcal{M} := \mathrm{diag}\{m_1\boldsymbol{E}, \boldsymbol{I}_{G1}, \cdots, m_n\boldsymbol{E}, \boldsymbol{I}_{Gn}\} \tag{12}$$

$$\dot{\boldsymbol{\xi}} := \begin{bmatrix}\dot{\boldsymbol{p}}_{G,1}^T & \boldsymbol{\omega}_1^T & \cdots & \dot{\boldsymbol{p}}_{G,n}^T & \boldsymbol{\omega}_n^T\end{bmatrix}^T \tag{13}$$

The relationship between $\dot{\boldsymbol{\xi}}$ and $\dot{\boldsymbol{q}}$ are represenetd as follows:

$$\dot{\boldsymbol{\xi}} = \mathcal{J}\dot{\boldsymbol{q}} \tag{14}$$

$$\mathcal{J} := \begin{bmatrix}\boldsymbol{J}_{G,1}^T & \boldsymbol{J}_{\omega,1}^T & \cdots & \boldsymbol{J}_{G,n}^T & \boldsymbol{J}_{\omega,n}^T\end{bmatrix}^T \tag{15}$$

It is observed from (10) that the inertia effect represented by $\mathcal{M}$ cannot be extracted from $\boldsymbol{\ell}$ because $\mathcal{M}$ is sandwitched by $\mathcal{A}$ and $\dot{\boldsymbol{\xi}}$.

B. Generalized Velocity and Force

Selection of the generalized velocity and force is not unique. We can select them so that the corresponding power is equal to that of the system. For example, we can select the generalized force corresponding to $\dot{\boldsymbol{\xi}}$ as

$$\mathcal{F} = \begin{bmatrix}\boldsymbol{f}_1^T & \boldsymbol{n}_1^T & \cdots & \boldsymbol{f}_n^T & \boldsymbol{n}_n^T\end{bmatrix}^T \tag{16}$$

Let $\boldsymbol{\tau}$ denote the generalized force corresponding to $\dot{\boldsymbol{q}}$. The power of the system is calculated as follows:

$$P = \dot{\boldsymbol{\xi}}^T\mathcal{F} = \dot{\boldsymbol{q}}^T\boldsymbol{\tau} \tag{17}$$

This relationship derives the virtual work principle, and we obtain

$$\boldsymbol{\tau} = \mathcal{J}^T\mathcal{F} \tag{18}$$

Suppose that the generalized velocity included in the AM is selected as $\overline{\boldsymbol{\omega}}$. It is necessary to satisfy the following equation with the corresponding generalized force $\overline{\boldsymbol{n}}$.

$$\dot{\boldsymbol{\xi}}^T\mathcal{F} = \dot{\boldsymbol{q}}^T\boldsymbol{\tau} = \overline{\boldsymbol{\omega}}^T\overline{\boldsymbol{n}} \tag{19}$$

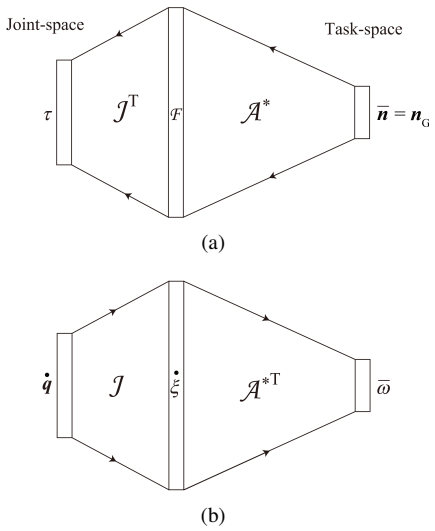


Fig. 2: Relationship among generalized (a) forces and (b) velocities.

In other words, we can select generalized velocity $\overline{\boldsymbol{\omega}}$ freely, but the resultant $\overline{\boldsymbol{n}}$ is automatically determined.

It is noted that the total moment around the COG $\boldsymbol{n}_G$ in (4) is rewritten by using $\mathcal{A}$ as follows:

$$\boldsymbol{n}_G = \mathcal{A}\mathcal{F} \tag{20}$$

We select $\overline{\boldsymbol{\omega}}$ as follows:

$$\overline{\boldsymbol{\omega}} = \mathcal{A}^{T*}\dot{\boldsymbol{\xi}} = \mathcal{A}^{T*}\mathcal{J}\dot{\boldsymbol{q}} \tag{21}$$

where $\mathcal{A}^*$ is the generalized inverse of $\mathcal{A}$.

$$\mathcal{A}\mathcal{A}^* = \boldsymbol{E} \tag{22}$$

In this case, the following relationship between $\overline{\boldsymbol{n}}$ and $\mathcal{F}$ is satisfied:

$$\mathcal{F} = \mathcal{A}^*\overline{\boldsymbol{n}}. \tag{23}$$

Substituting (23) into (20) yields

$$\boldsymbol{n}_G = \mathcal{A}\mathcal{F} = \mathcal{A}\mathcal{A}^*\overline{\boldsymbol{n}} = \overline{\boldsymbol{n}}. \tag{24}$$

This result implies that we can select $\overline{\boldsymbol{\omega}}$ so that the corresponding generalized force $\overline{\boldsymbol{n}}$ is equal to the net torque on the COG. The schematic diagram about the relationship among generalized forces and velocities in joint-space and the corresponding terms in task-space is shown in Fig. 2.

C. Candidates of $\mathcal{A}^*$

One of candidates of $\mathcal{A}^*$ is the pseudo-inverse of $\mathcal{A}$ define as follows:

$$\mathcal{A}^\sharp = \mathcal{A}^T(\mathcal{A}\mathcal{A}^T)^{-1}. \tag{25}$$

Another candidate is the weighting pseudo-inverse. When the inertia matrix $\mathcal{M}$ is selected as the weight, the pseudo-inverse is represented as follows:

$$\mathcal{A}^\dagger = \mathcal{M}\mathcal{A}^T(\mathcal{A}\mathcal{M}\mathcal{A}^T)^{-1}. \tag{26}$$

The physical meanings of the selection of $\mathcal{A}^*$ are summarized as follows:

- When we select $\mathcal{A}^\sharp$, the generalized velocity does not include the inertia effect.
- When we select $\mathcal{A}^\dagger$, the corresponding velocity $\overline{\boldsymbol{\omega}}$ is calculated as follows:

  $$\overline{\boldsymbol{\omega}} = (\mathcal{A}\mathcal{M}\mathcal{A}^T)^{-1}\mathcal{A}\mathcal{M}\mathcal{J}\dot{\boldsymbol{q}} = \boldsymbol{I}_G^{-1}\boldsymbol{J}_{\mathrm{AM}}\dot{\boldsymbol{q}} = \boldsymbol{I}_G^{-1}\boldsymbol{\ell}$$

  In the above calculation, we used

  $$\boldsymbol{I}_G = \mathcal{A}\mathcal{M}\mathcal{A}^T. \tag{27}$$

  Therefore,

  $$\boldsymbol{\omega}_G = \overline{\boldsymbol{\omega}} \tag{28}$$

  is satisfied, which means that $\boldsymbol{\omega}_G$ is the genealized velocity.

IV. Viscoelasticity on Centroidal Dynamics

A. Angular Momentum Damping and Virtual Work Principle

One of controls using the AM is a damping control to reduce the $\boldsymbol{\ell}$, represented as follows:

$$\boldsymbol{n}_G = \boldsymbol{D}_\ell \Delta\boldsymbol{\ell} \tag{29}$$

where $\boldsymbol{D}_\ell \in \mathbb{R}^{3\times 3}$ is a viscosity matrix of the AM. We consider to achieve $\boldsymbol{D}_\ell$ by the joint-space viscosity given as follows:

$$\boldsymbol{\tau} = \boldsymbol{D}_\theta \Delta\dot{\boldsymbol{\theta}} \tag{30}$$

where $\boldsymbol{D}_\theta \in \mathbb{R}^{n\times n}$ is the viscosity matrix in the joint-space.

The relationship between (29) and (30) is derived as follows. From (29), we have

$$\begin{aligned}\boldsymbol{D}_\ell^{-1}\boldsymbol{n}_G = \Delta\boldsymbol{\ell} = \boldsymbol{J}_{\mathrm{AM}}\Delta\dot{\boldsymbol{\theta}} &= \boldsymbol{J}_{\mathrm{AM}}\boldsymbol{D}_\theta^{-1}\boldsymbol{\tau} \\ &= \boldsymbol{J}_{\mathrm{AM}}\boldsymbol{D}_\theta^{-1}\boldsymbol{J}_{A*}^T\boldsymbol{n}_G\end{aligned} \tag{31}$$

In the above transformation, we used

$$\boldsymbol{\tau} = \boldsymbol{J}_{A*}^T\boldsymbol{n}_G, \tag{32}$$

and define

$$\boldsymbol{J}_{A*} := \boldsymbol{A}^{T*}\mathcal{J}. \tag{33}$$

Therefore, the condition that (31) is satisfied for arbitrary $\boldsymbol{n}_G$ is represented as follows:

$$\boldsymbol{D}_\ell^{-1} = \boldsymbol{J}_{\mathrm{AM}}\boldsymbol{D}_\theta^{-1}\boldsymbol{J}_{A*}^T \tag{34}$$

Note that $\boldsymbol{D}_\ell$ is not *viscosity* for velocity but a matrix containing the inertia effect. We can summarize the selection of $\boldsymbol{A}^*$ and $\boldsymbol{J}_{A*}$ in (34) as follows:

- In the case of $\boldsymbol{A}^* = \boldsymbol{A}^\sharp$, the inertia effect is included only in $\boldsymbol{J}_{\mathrm{AM}}$ as $\boldsymbol{J}_{A\sharp}$ is based only on the geometrical structure.
- In the case of $\boldsymbol{A}^* = \boldsymbol{A}^\dagger$, the inertia effect is included not only in $\boldsymbol{J}_{\mathrm{AM}}$ but also in $\boldsymbol{J}_{A\dagger}$. In other words, the inertia effect is *double-counted*.

B. Control Based on COG-ZMP Model

By using zero moment point (ZMP), we can rewrite (1) as follows [18]:

$$\ddot{\boldsymbol{p}}_{\mathrm{G}} = \omega^2(\boldsymbol{p}_{\mathrm{G}} - \boldsymbol{p}_{\mathrm{Z}}) - \boldsymbol{S}\boldsymbol{n}_G - \boldsymbol{g} \tag{35}$$

where $\boldsymbol{p}_Z$ is the ZMP position, and $\boldsymbol{\nu}$ is the unit vector normal to the plane on which the ZMP is defined. Usually, $\boldsymbol{\nu}$ is set as $\boldsymbol{\nu} = [0\ 0\ 1]^{\mathrm{T}}$. We also define ω and $\boldsymbol{S}$ as follows:

$$\omega := \sqrt{\frac{\boldsymbol{\nu}^{\mathrm{T}}(\ddot{\boldsymbol{p}}_{\mathrm{G}} + \boldsymbol{g})}{\boldsymbol{\nu}^{\mathrm{T}}(\boldsymbol{p}_{\mathrm{G}} - \boldsymbol{p}_{\mathrm{Z}})}} \tag{36}$$

$$\boldsymbol{S} := \frac{[\boldsymbol{\nu}\times]}{m\boldsymbol{\nu}^{\mathrm{T}}(\boldsymbol{p}_{\mathrm{G}} - \boldsymbol{p}_{\mathrm{Z}})} \tag{37}$$

We transform (2) and (35) into a state equation. We select the state variable $\boldsymbol{x}$ and control input $\boldsymbol{u}$ as follows:

$$\boldsymbol{x} = \begin{bmatrix} \boldsymbol{p}_{\mathrm{G}} \\ \dot{\boldsymbol{p}}_{\mathrm{G}} \\ \boldsymbol{\ell} \end{bmatrix}, \quad \boldsymbol{u} = \begin{bmatrix} \boldsymbol{p}_Z \\ \boldsymbol{n}_G \end{bmatrix} \tag{38}$$

Equations (2) and (35) are transformed as follows:

$$\dot{\boldsymbol{x}} = \boldsymbol{A}\boldsymbol{x} + \boldsymbol{B}\boldsymbol{u} + \boldsymbol{G}\boldsymbol{w}, \tag{39}$$

$$\boldsymbol{A} := \begin{bmatrix} \boldsymbol{O} & \boldsymbol{E} & \boldsymbol{O} \\ \omega^2\boldsymbol{E} & \boldsymbol{O} & \boldsymbol{O} \\ \boldsymbol{O} & \boldsymbol{O} & \boldsymbol{O} \end{bmatrix}, \tag{40}$$

$$\boldsymbol{B} := \begin{bmatrix} \boldsymbol{O} & \boldsymbol{O} \\ -\omega^2\boldsymbol{E} & -\boldsymbol{S} \\ \boldsymbol{O} & \boldsymbol{E} \end{bmatrix}, \quad \boldsymbol{G} := \begin{bmatrix} \boldsymbol{O} & \boldsymbol{O} \\ \dfrac{1}{m}\boldsymbol{E} & \boldsymbol{O} \\ \boldsymbol{O} & \boldsymbol{E} \end{bmatrix} \tag{41}$$

where $\boldsymbol{w} \in \mathbb{R}^6$ is the external wrench applied to the COG. When there is no external force except for the gravity, we have $\boldsymbol{w} = [-m\boldsymbol{g}^T\ \boldsymbol{0}^T]^T$.

A standing balance control can be achieved by a state feedback given as follows:

$$\boldsymbol{u} = \boldsymbol{u}_{ref} + \boldsymbol{F}(\boldsymbol{x}_{ref} - \boldsymbol{x}) \tag{42}$$

where $\boldsymbol{F}$ is a state feedback gain. We can utilize the linear quadratic regulator as $\boldsymbol{F}$. The other candidate of $\boldsymbol{F}$ is represented as follows:

$$\boldsymbol{F} = \begin{bmatrix} \boldsymbol{F}_{11} & \boldsymbol{F}_{12} \\ \boldsymbol{F}_{21} & \boldsymbol{F}_{22} \end{bmatrix} = \begin{bmatrix} \mathrm{diag}\{\alpha_i\} \\ \mathrm{diag}\{\beta_i\} \end{bmatrix} \begin{bmatrix} \boldsymbol{E} & \frac{1}{\omega}\boldsymbol{E} \end{bmatrix}. \tag{43}$$

where α_i and $\beta_i (i = 1, 2, 3)$ are gain parameters for $\boldsymbol{p}_Z$ and $\boldsymbol{n}_G$, respectively. This feedback gain is of the capture point [19] and maximizes the stability region [18].

C. Centroidal Viscoelasticity

In a manner similar to [16], we can transform (43) into the viscoelasticity on the COG.

$$\begin{bmatrix} \boldsymbol{f}_G \\ \boldsymbol{n}_G \end{bmatrix} = \begin{bmatrix} \boldsymbol{f}_{G,ref} \\ \boldsymbol{n}_{G,ref} \end{bmatrix} + \begin{bmatrix} \boldsymbol{K}_{G1} \\ \boldsymbol{K}_{G2} \end{bmatrix} \Delta\boldsymbol{p}_G + \begin{bmatrix} \boldsymbol{D}_{G1} \\ \boldsymbol{D}_{G2} \end{bmatrix} \Delta\dot{\boldsymbol{p}}_G \tag{44}$$

$$\boldsymbol{K}_{Gi} := -m\omega^2(\boldsymbol{E} + \boldsymbol{F}_{i1}) \tag{45}$$

$$\boldsymbol{D}_{Gi} := -m\omega^2\boldsymbol{F}_{i2} \tag{46}$$

where

1) $(\boldsymbol{K}_{G1}, \boldsymbol{D}_{G1})$ is viscoelasticity between the COG and $\boldsymbol{f}_G$; and
2) $(\boldsymbol{K}_{G2}, \boldsymbol{D}_{G2})$ is viscoelasticity between the COG and $\boldsymbol{n}_G$.

Moreover, we can superpose the AM damping given by (29) on (44) as follows:

$$\begin{bmatrix} \boldsymbol{f}_G \\ \boldsymbol{n}_G \end{bmatrix} = \begin{bmatrix} \boldsymbol{f}_{G,ref} \\ \boldsymbol{n}_{G,ref} \end{bmatrix} + \begin{bmatrix} \boldsymbol{K}_{G1} \\ \boldsymbol{K}_{G2} \end{bmatrix} \Delta\boldsymbol{p}_G + \begin{bmatrix} \boldsymbol{D}_{G1} & * \\ \boldsymbol{D}_{G2} & \boldsymbol{D}_\ell \end{bmatrix} \begin{bmatrix} \Delta\dot{\boldsymbol{p}}_G \\ \Delta\boldsymbol{\ell} \end{bmatrix} \tag{47}$$

where $*$ represents the effect of AM term on net force $\boldsymbol{f}_G$, expressed as $-m\boldsymbol{S}\boldsymbol{D}_\ell$. In this paper, we call the viscoelasticity given by (47) as *centroidal viscoelasticity*.

We consider the relationship between the centroidal viscoelasticity and the joint-space viscoelasticity given by

$$\boldsymbol{\tau} = \boldsymbol{\tau}_{\mathrm{ref}} + \boldsymbol{K}_\theta\Delta\boldsymbol{\theta} + \boldsymbol{D}_\theta\Delta\dot{\boldsymbol{\theta}}. \tag{48}$$

From the virtual work principle, we can derive the following relationships:

$$\begin{bmatrix} \boldsymbol{K}_{G1} \\ \boldsymbol{K}_{G2} \end{bmatrix} \boldsymbol{J}_G\boldsymbol{K}_\theta^{-1} \begin{bmatrix} \boldsymbol{J}_G^T & \boldsymbol{J}_{A*}^T \end{bmatrix} = \boldsymbol{E} \tag{49}$$

$$\begin{bmatrix} \boldsymbol{J}_G \\ \boldsymbol{J}_{AM} \end{bmatrix} \boldsymbol{D}_\theta^{-1} \begin{bmatrix} \boldsymbol{J}_G^T & \boldsymbol{J}_{A*}^T \end{bmatrix} = \begin{bmatrix} \boldsymbol{D}_{G1} & * \\ \boldsymbol{D}_{G2} & \boldsymbol{D}_\ell \end{bmatrix}^{-1} \tag{50}$$

where $\boldsymbol{J}_G$ is the Jacobian matrix of the COG velocity of whole body.

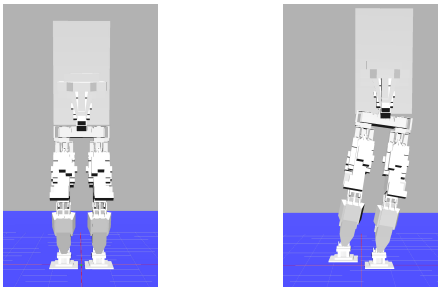
At last, we can use the compliance optimization through statics-based method or dynamics-based method [20] to solve the joint viscoelasticity under constraints (49) and (50).

V. Validation by Forward Dynamics Simulation

A. Simulation Environment

We validate the proposed method through forward dynamics simulations assuming a hydro-statically driven humanoid robot, Hydra (180cm, 74kg, 14 DOFs) [21]. In the simulations, we compare the following three methods:

1) Case1 RVC method only considering the COG viscoelascicity [22]
2) Case2 Proposed method with $\boldsymbol{A}^* = \boldsymbol{A}^\sharp$
3) Case3 Proposed method with $\boldsymbol{A}^* = \boldsymbol{A}^\dagger$



(a) double support (b) single support

Fig. 3: Initial posture in the simulations of balance control with (a) double-support and (b) single support states.

B. Balance Control with Double Support

In double support simulation, the robot stands on two feet to keep balance under external impact. Fig. 3(a) shows the situation of this simulation. In this simulation, we mainly focus on validating the AM damping control performance of the proposed method than previous RVC. The feedback gains $\alpha_i (i = 1, 2, 3)$ are -1.5, -1.5 and -1000 for all three cases, whereas $\beta_i (i = 1, 2, 3)$ are not used. The AM viscosity matrix D_ℓ is set as diag$\{10\}$. Fig. 4(a)-(d) include the simulation results of COG position, COG velocity, ZMP position in x-direction, and AM in y-direction, under a 10Ns impact (500N in 0.02s) applied on the waist link in $+x$ direction at about 2s (the animation is shown in accompanied video). In this result, we can see Case2 has the more rapid convergency in AM and COG; Case3 has the similar tendency but with large oscillation on AM. In the accompanied video, we can find the robot rotates its waist to control AM in Case2 and Case3, but not in Case1. Accordingly, we consider Case2 has the effectiveness in AM convergency, which validates the feasibility of proposed method in AM damping control.

C. Balance Control with Single Support

In single support simulation, the robot stands on the left foot with swinging right foot in the air, and needs to keep balance under an external impact acting on the body. Fig. 3(b) shows the situation of this simulation. In this case, the robot has a swing leg which helps to achieve decoupled AM control than in double support case. In detail, the feedback gains $\alpha_i (i = 1, 2, 3)$ are -1.5, -1.5 and -1000 for all three cases, $\beta_i (i = 1, 2, 3)$ are -1.5, -1.5 and -1.5 for only Case2 and Case3, and D_l set as diag$\{10\}$. The respective control performances of three cases under a 20Ns impact (1000N in 0.02s) applied on the waist link in $+x$ direction at about 2s are shown in Fig. 5, including COG position, COG velocity, ZMP position in x-direction, and AM in y-axis (the animation is shown in accompanied video). Intuitively we can see that, Case2 and Case3 have smaller deviation in COG and higher speed convergency of AM after impact than Case1, while Case3 has more oscillation in ZMP than Case2.

We also tested to apply a 20Ns impact (1000N in 0.02s) on the right foot during single support, and the results are shown in Fig. 6 (the animation is shown in accompanied video). As is demonstrated in these figures, Case2 and Case3 have the smoother convergency in COG than Case1, though have larger deviation after impact. Also, in Case2 and Case3, the AM fluctuation is smaller than Case1.

Generally, in the above double and single support simulation, compared with previous RVC method in Case1, the proposed methods Case2 and Case3 have better convergency in COG state and AM; then compared with Case2, Case3 is more easily to oscillate. Thus we conclude that because of the AM-included state feedback control and the inertia-decoupled centroidal viscoelasticity, Case2 has the relatively better performance in COG and AM control than Case1 and Case3, which can improve the ability of push recovery for the humanoid robot. As for the undesirable performance in Case3, we consider the reason is that *double-counted* inertia introduces an extra inertia-related weight on centroidal viscoelasticity resolution, making the feedback gain deviate from original setting, which causes the oscillation in centroidal state.

D. Balance Control of Single-leg Landing Motion After Hop

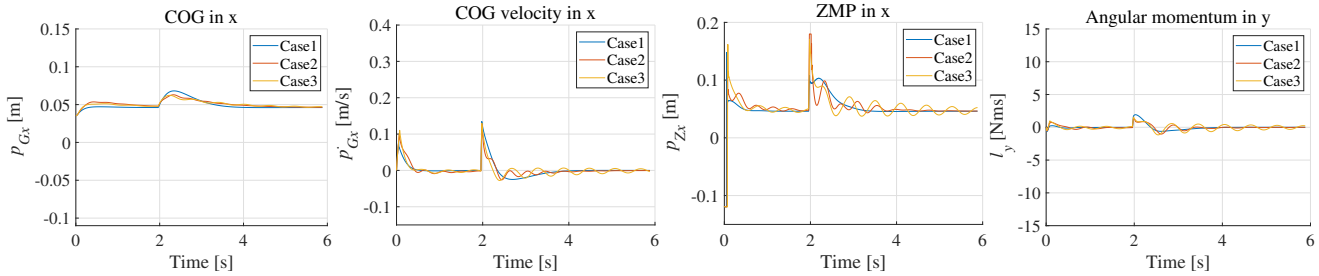
After preliminary validation in standing motion control under an external impact, here we test the proposed method in balance control of landing motion after a hop. In this simulation, the robot firstly stands on single leg, then take off with this supporting leg, and touch down with the same leg to keep the balance quickly. The generation of motion in take-off phase is according to the running gait generator in [23]. During the take-off and flight phase the whole-body of robot is controlled directly by joint PD control, and in touch-down phase the previous RVC and the proposed method will be applied respectively, with the same coefficient setting as in single support simulation. Due to the direct PD control without explicit COG or AM control in take-off phase, the robot has undesired COG and AM perturbation during flight phase till touch-down, which just provides an unbalancing condition to test our method in balancing control. Therefore, the aim of this simulation is to test the applicability and robustness of different methods in more complicated situation, such as landing with impact mitigation. Additionally, due to the undesired performance of Case3 in the above tests, we only compare Case1 and Case2 here.

Fig. 7(a)-(d) include the simulation results (the animation is shown in accompanied video). Note that the motions in the first 1.4s are totally the same under a joint PD control, which cause the unpredictable fluctuation on COG velocity and AM for final landing. In the landing motion we can see Case2 still has a better convergency performance in both COG and AM state. By the way, there is a small difference of final equilibrium value of COG between Case1 and Case2, but these two values are both within the limiation of foot sole, which means they are still balanced.

VI. Conclusion

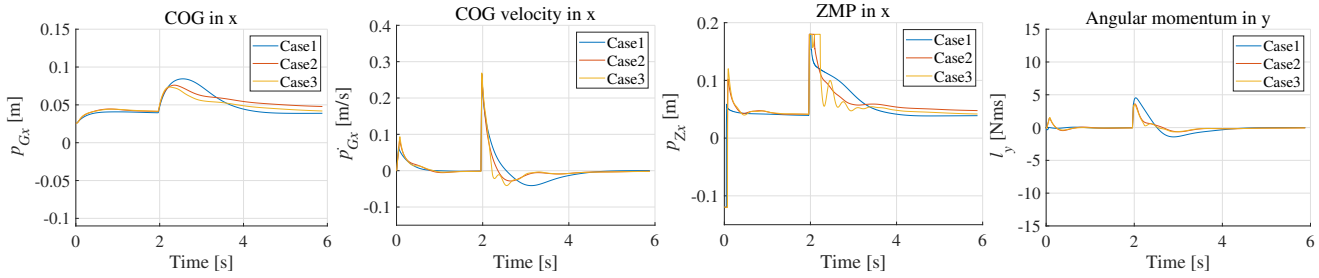
This study involved decoupling of inertia term in angular momentum of humanoid robot, and its corresponding application to extending previous resolved viscoelasticity control into centroidal viscoelasticity. Through the proposed definition of generalized velocity, we achieved AM control and COG control through AM term, based on COG-ZMP model. The validation of the proposed method was presented in forward dynamics simulation, proving the effectiveness in balance control. Compared with the other AM-considered control method, the proposed method in this paper has advantage in decoupling and analyticity, because it can separate the inertia term from generalized angular velocity and calculate the required joint-space compliance for AM-considered control analytically.

A future study will focus on more dynamic motion, and combine centroidal viscoelasticity with other body tasks to realize more complicated assignment.



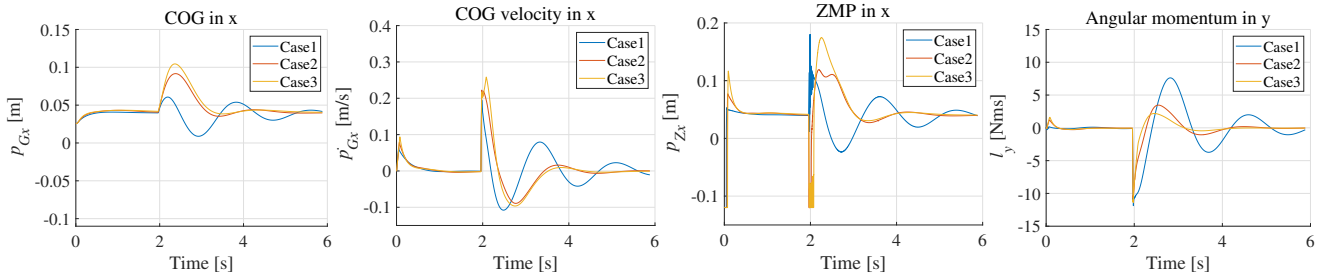
(a) COG position x_G (b) COG velocity $\dot{x}_G$ (c) ZMP position x_Z (d) AM ℓ_y

Fig. 4: Simulation results of double support balancing with only AM damping control under impact on waist (10Ns, at 2s).



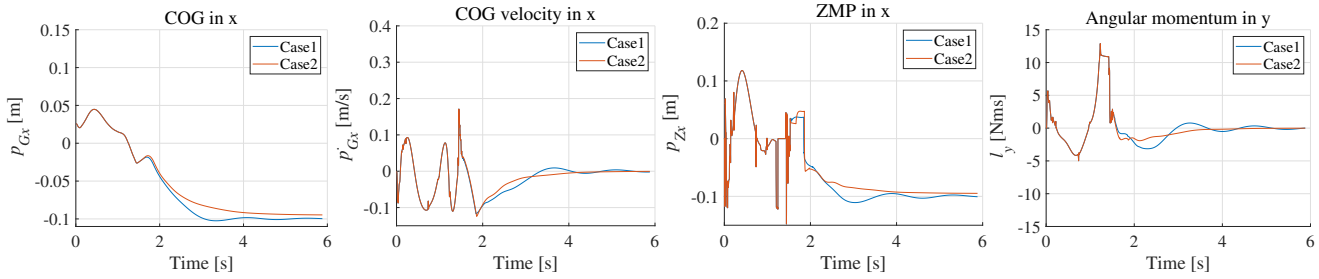
(a) COG position x_G (b) COG velocity $\dot{x}_G$ (c) ZMP position x_Z (d) AM ℓ_y

Fig. 5: Simulation results of single support balancing under impact on waist (20Ns, at 2s).



(a) COG position x_G (b) COG velocity $\dot{x}_G$ (c) ZMP position x_Z (d) AM ℓ_y

Fig. 6: Simulation results of single support balancing under impact on swinging foot (20Ns, at 2s).



(a) COG position x_G (b) COG velocity $\dot{x}_G$ (c) ZMP position x_Z (d) AM ℓ_y

Fig. 7: Simulation results of single-leg landing after hop (robot touching the ground at about 1.4s).

REFERENCES

[1] R. Blickhan, "The spring-mass model for running and hopping," *Journal of biomechanics*, vol. 22, no. 11-12, pp. 1217–1227, 1989.

[2] S. Kajita and K. Tani, "Study of dynamic biped locomotion on rugged terrain-derivation and application of the linear inverted pendulum mode," in *Proceedings. 1991 IEEE International Conference on Robotics and Automation*. IEEE Computer Society, 1991, pp. 1405–1406.

[3] J. E. Pratt and S. V. Drakunov, "Derivation and application of a conserved orbital energy for the inverted pendulum bipedal walking model," in *Proceedings 2007 IEEE International Conference on Robotics and Automation*. IEEE, 2007, pp. 4653–4660.

[4] F. Miyazaki and S. Arimoto, "A control theoretic study on dynamical biped locomotion," 1980.

[5] D. E. Orin, A. Goswami, and S.-H. Lee, "Centroidal dynamics of a humanoid robot," *Autonomous Robots*, vol. 35, no. 2-3, pp. 161–176, jun 2013.

[6] T. Sugihara, "Mobility Enhancement Control of Humanoid Robot based on Reaction Force Manipulation via Whole Body Motion," Ph.D. dissertation, University of Tokyo, 2004.

[7] S. Kajita, F. Kanehiro, K. Kaneko, K. Fujiwara, K. Harada, K. Yokoi, and H. Hirukawa, "Resolved momentum control: humanoid motion planning based on the linear and angular momentum," in *Proceedings of IEEE/RSJ International Conference on Intelligent Robots and Systems*, vol. 2, 2003, pp. 1644–1650.

[8] A. Miyata, S. Miyahara, and D. N. Nenchev, "Walking with Arm Swinging and Pelvis Rotation Generated with the Relative Angular Acceleration," in *IEEE Robotics and Automation Letters*, vol. 5, no. 1, 2020, pp. 151–158.

[9] A. Saccon, S. Traversaro, F. Nori, and H. Nijmeijer, "On Centroidal Dynamics and Integrability of Average Angular Velocity," *IEEE Robotics and Automation Letters*, vol. 2, no. 2, pp. 943–950, 2017.

[10] Z. Aftab, T. Robert, and P.-B. Wieber, "Ankle, hip and stepping strategies for humanoid balance recovery with a single model predictive control scheme," in *2012 12th IEEE-RAS International Conference on Humanoid Robots (Humanoids 2012)*. IEEE, 2012, pp. 159–164.

[11] M. Shafiee-Ashtiani, A. Yousefi-Koma, M. Shariat-Panahi, and M. Khadiv, "Push recovery of a humanoid robot based on model predictive control and capture point," in *2016 4th International Conference on Robotics and Mechatronics (ICROM)*. IEEE, 2016, pp. 433–438.

[12] K. Guan, K. Yamamoto, and Y. Nakamura, "Push recovery by angular momentum control during 3d bipedal walking based on virtual-mass-ellipsoid inverted pendulum model," in *2019 IEEE-RAS 19th International Conference on Humanoid Robots (Humanoids)*. IEEE, 2019, pp. 120–125.

[13] C. McGreavy, K. Yuan, D. Gordon, K. Tan, W. J. Wolfslag, S. Vijayakumar, and Z. Li, "Unified push recovery fundamentals: Inspiration from human study," in *2020 IEEE International Conference on Robotics and Automation (ICRA)*. IEEE, 2020, pp. 10 876–10 882.

[14] J. Ding, S. Xin, T. L. Lam, and S. Vijayakumar, "Versatile locomotion by integrating ankle, hip, stepping, and height variation strategies," in *2021 IEEE International Conference on Robotics and Automation*. Institute of Electrical and Electronics Engineers (IEEE), 2021.

[15] K. Yamamoto, "Resolved COG Viscoelasticity Control of Humanoid," in *Proc. of IEEE/RSJ IROS*, 2016.

[16] ——, "Resolved Multiple-Viscoelasticity Control for a Humanoid," *IEEE Robotics and Automation Letters*, vol. 3, no. 1, pp. 44–51, 2017.

[17] D. N. Nenchev, "The Momentum Equilibrium Principle: Foot Contact Stabilization with Relative Angular Momentum/Velocity," in *IEEE-RAS International Conference on Humanoid Robots*, 2019, pp. 17–24.

[18] K. Yamamoto, T. Kamioka, and T. Sugihara, "Survey on model-based biped motion control for humanoid robots," *Advanced Robotics*, vol. 34, no. 21-22, pp. 1353–1369, 2020.

[19] T. Sugihara, "Standing stabilizability and stepping maneuver in planar bipedalism based on the best com-zmp regulator," in *2009 IEEE International Conference on Robotics and Automation*. IEEE, 2009, pp. 1966–1971.

[20] K. Yamamoto and Y. Nakamura, "Compliance optimization considering dynamics for whole-body control of a humanoid," in *2019 International Symposium on Robotics Research*, 2019.

[21] T. Ko, K. Murotani, K. Yamamoto, and Y. Nakamura, "Whole-body Compliant Motion by Sensor Integration of an Eha-Driven Humanoid Hydra," *International Journal of Humanoid Robotics*, vol. 2150002, pp. 1–26, 2021.

[22] K. Yamamoto, "Humanoid Motion Analysis and Control based on COG Viscoelasticity," *Advanced Robotics*, vol. 31, no. 7, pp. 341–354, 2017.

[23] T. Sugihara, K. Imanishi, T. Yamamoto, and S. Caron, "3d biped locomotion control including seamless transition between walking and running via 3d zmp manipulation," in *The 2021 IEEE International Conference on Robotics and Automation (ICRA)*. IEEE, 2021, pp. 6258–6263.